Investigation of microstructure and texture evolution in an AZ31/Mg-Gd alloy hybrid metal fabricated by high-pressure torsion

Ouarda Ould Mohamed[1], Hiba Azzeddine[1,*], Yi Huang[2,3], Thierry Baudin[4], Piotr Bazarnik[5], François Brisset[4], Megumi Kawasaki[6], Terence G. Langdon[2]

[1] Laboratory of Materials and Renewable Energy, Faculty of Sciences, Mohamed Boudiaf University, 28000 M'sila, Algeria
[2] Materials Research Group, Department of Mechanical Engineering, University of Southampton, Southampton SO17 1BJ, UK
[3] Department of Design and Engineering, Faculty of Science and Technology, Bournemouth University, Poole, Dorset BH12 5BB, UK
[4] Université Paris-Saclay, CNRS, Institut de chimie moléculaire et des matériaux d'Orsay, 91405 Orsay, France
[5] Warsaw University of Technology, Faculty of Materials Science and Engineering, Woloska 141, 02-507, Poland
[6] School of Mechanical, Industrial and Manufacturing Engineering, Oregon State University, Corvallis, OR 97331, USA
* Corresponding author: Prof. Hiba Azzeddine, hiba.azzeddine@univ-msila.dz

Abstract

High-pressure torsion (HPT) processing was successfully applied to fabricate a novel hybrid material from separate discs of AZ31 (Mg-3Al-1Zn, wt.%) and Mg-0.6Gd (wt.%) alloys by straining through numbers of rotations, *N*, of 1/4, 1/2, 5, 10 and 20 turns at room temperature. The microstructure and texture were investigated near the bonding interface through the disc diameter using Electron Backscatter Diffraction (EBSD), Scanning Electron Microscopy (SEM) and Transmission Electron Microscopy (TEM). The microstructure exhibited two grain refinement regimes with the first occurring during an equivalent strain range, ε_{eq}, of ~0.3–72 and the second during ε_{eq} from ~72–517. The general texture changed from B-fiber to Y-fiber and C_2-fiber through the HPT processing. The resultant microstructures and textures of this hybrid alloy are examined separately for the AZ31 and Mg-0.6Gd alloys and found controlled by the presence of twinning, slip systems and second phases and the occurrence of different dynamic recrystallization mechanisms.

Keywords: High-pressure torsion; Hybrid metal; Magnesium; Microstructure; Rare-earth; Texture

1. Introduction

It is now well recognized that high-pressure torsion (HPT) is one of the most efficient techniques of severe plastic deformation (SPD) that can produce materials with excellent grain refinement and outstanding mechanical properties at room temperature (RT) [1]. Moreover, HPT processing allows materials having low crystal symmetry, such as magnesium-based alloys having hexagonal close-packed (HCP) structures, to be deformed at room temperature [2-8]. Significant grain refinement, to the range of ~110-250 nm, was reported using HPT processing in several Mg-based alloys [4, 5, 8-12].

The mechanism responsible for grain refinement in these Mg-based alloys is dynamic recrystallization (DRX) due to the lack of a sufficient number of active slip systems [13]. Specifically, it is a discontinuous DRX process in which an array of new fine grains form along the original grain boundaries in a necklace-like structure in the process known as a strain-induced boundary migration (SIBM) mechanism [13, 14]. In this mechanism, the bulging of the grain boundaries is caused directly by the difference in the dislocation density on either side of the boundary. The misorientations between the bulges and the deformed grains then increases with increasing strain and this leads to the formation of sub-grain boundaries which ultimately transform to new fine grains having high-angle grain boundaries (HAGBs). These new grains gradually consume the deformed grains leading to an ultrafine-grained microstructure [13, 14]. Consequently, the distribution of the misorientations in the grain boundaries is not altered through the deformation and grain refinement [7, 15]. The majority of HCP materials processed by HPT develop a basal texture (B-fiber), where the basal {0002} planes of the lattices in the grains become parallel to the normal shear plane [16]. Nevertheless, the presence of alloying elements such as rare earth (RE) elements in Mg-based alloys, and the distribution of second phases, cause deviations in the basal texture from its ideal position [7, 16, 17].

Recent reports have demonstrated the feasibility of using HPT processing at RT to synthesize new hybrid alloys such as the Cu–Ni [18], Ag-Cu [19], Al-Cu [20], Al-Mg [21, 22], Al-Ti [23], V-Zr [24] and Zn-Mg [25] systems which are formed through solid-state reactions. An earlier report summarized the formation of unique alloy systems from separate bulk metals through the application of HPT [26] and it is evident that, well below the application of ultra-severe plastic deformation [27], a heterogeneous microstructure is formed with ultrafine multi-layered structures in the central areas of HPT disc samples and with nano-layered intermetallic phases embedded within mixed zones near the edges of the sample.

The homogeneity developed in these hybrid systems is controlled by the HPT processing conditions including the amount of the imposed strain, the processing temperature and any post-deformation heat treatment [18, 23, 24, 28-30]. To date, the scientific investigations have focused primarily on exploring the mechanical properties, as in tensile testing and the Vickers microhardness, together with the corrosion and tribological properties of the fabricated hybrid systems. The results confirm that HPT processing is a promising technique for bonding dissimilar materials at RT and for fabricating new materials for different structural applications. Currently, most published data are based on characterizing the microstructures of the mixed layers and the formation of the intermetallic phases during HPT processing of dissimilar materials [20, 23-25, 30-33].

Following a comprehensive examination of these earlier results, the present work was undertaken specifically to explore the potential for bonding two alloys having similar Mg matrices, namely AZ31 (Mg-3Al-1Zn, wt.%) and Mg-0.6Gd (wt.%) alloys, through the application of HPT processing.

Lightweight Mg-Al based alloys such as AZ31 alloy are very promising candidates to be used for weight reduction in transportations (aerospace and automotive) and the electronics industries and also as potential biodegradable implant materials in biomedical applications due to their low density, high specific strength and biodegradability [34-39]. However, Mg-Al based alloys usually suffer from poor ductility and a rapid corrosion rate which significantly limits their industrial applications [34, 39, 40]. Mg alloyed with RE elements is now considered as an efficient route for improving the ductility of Mg-based alloys without compromising their strength [41-43]. Hence, the fabricates of a new generation of Mg hybrid materials with similar Mg matrices using HPT processing could be new strategy to achieve the desired combinations of properties and enhance the lightweight characteristics in order to extend the use of Mg-based alloys in different structural applications. It is important to note that, to date, there are no similar investigations describing the joining of dissimilar Mg-based alloys using HPT processing. Accordingly, the present research was initiated to examine the microstructure and texture development near the bonding interface in AZ31 and Mg-0.6Gd alloys using electron backscatter diffraction (EBSD) and transmission electron microscopy (TEM). The results are discussed with reference to the initial conditions and the separate microstructural and textural changes produced in the AZ31 and Mg-0.6Gd alloys.

2. Experimental materials and procedures

Sheets of hot-rolled AZ31 and an as-cast Mg-0.6Gd alloy were supplied by the Magnesium Innovations Center (MagIC, Germany) and the Institute of Physical Metallurgy and Materials Physics (RWTH-Aachen University, Germany), respectively. The microstructure of the as-received alloys was revealed using optical microscopy after grinding with progressively finer SiC papers followed by electropolishing with 5:3-part ethanol and phosphoric acid for 30 min under a 3V applied voltage and etching at room temperature in an acetic-Nital solution (5% HNO_3, 15% acetic acid, 20% distilled water and 60% ethanol) for 3 s.

Discs with diameters of 10 mm and thicknesses of 0.85 mm were machined and prepared from both alloys. The AZ31 disc was placed on the lower anvil in the HPT facility and then the Mg-0.6Gd disc was placed on top as illustrated in Figure 1a and the two disks were processed together by HPT at RT for numbers of HPT turns, N, of 1/4, 1/2, 5, 10 and 20 under quasi-constrained conditions [44, 45]. The HPT discs were processed under a pressure of 6.0 GPa with a rotational speed of 1 rpm and care was taken to ensure there was no significant slippage during the HPT processing [46]. The equivalent strain, ε_{eq}, imposed during HPT is given by the relationship [47]:

$$\varepsilon_{eq} = \frac{2\pi N r}{\sqrt{3}h} \tag{1}$$

where r is the radial distance from the centre of the disc and h is the thickness of the disc.

All microstructural observations and texture and microhardness measurements were undertaken on the cross-sectional (CD-SD) planes of the HPT discs where the shear reference frame is defined as the shear direction (SD), rotational direction (RD) and compression direction (CD). Following the HPT processing the discs were cut into two halves along their mid-plane.

The EBSD measurements were performed near the centre ($r \approx 0.2$ mm), at the mid-radius position ($r \approx 2.5$ mm) and at the edge ($r \approx 4.5$ mm) of the mid-thickness plane of the HPT-processed discs as illustrated in Figure 1 using a TSL-EDAX-Hikari system mounted on a scanning electron microscope (FEG-SEM ZEISS Supra 55 VP) operating at 20 kV. Data collected from scanned areas of 40×40 μm^2 with a 0.1 μm step size were managed by the Orientation Imaging Microscopy OIM$^{\text{TM}}$ software. Grain size data were obtained using a grain tolerance angle of 5° and a minimum grain size of 5 pixels. All datum points with a confidence index (CI) < 0.05 were excluded from the quantitative analyses [48]. In addition, spurious boundaries with misorientation angles $\theta < 2°$ were excluded from the EBSD maps to avoid any orientation noise. The mean grain size was measured using the equivalent diameter approach.

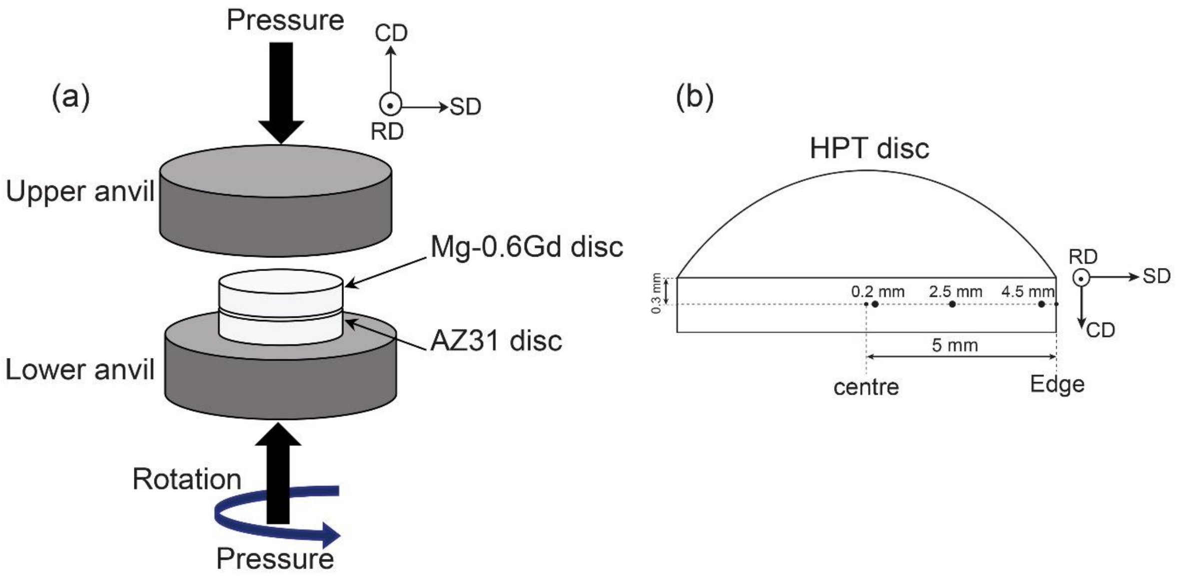

Figure 1: An illustration showing: (a) HPT processing and (b) the position for the EBSD on the vertical cross-section of the HPT disc. SD, CD, and RD are the coordinate systems.

The grain orientation spread (GOS) approach in the OIM™ software was used for the identification of dynamic recrystallized grains. The GOS is defined as the average deviation between the orientation of each point in the grain and the average orientation of the grain, where grains with GOS < 1° are considered as fully recrystallized [49].

MTEX software was used to analyze the evolution of texture by calculating the orientation distribution function (ODF) using the harmonic method (L = 22) and a Gaussian function with a half-width of 5° to model each orientation [50].

A field emission gun scanning electron microscope (FEG-SEM ZEISS Gemini) equipped with an energy dispersive spectrometry (EDS) system in backscattering (BSE) mode operating at 15 kV was used for the microstructural investigation and to obtain the chemical element mapping of samples processed for *N* = 1/4 turn. Another SEM (Hitachi SU8000) was used to analyse the microstructures at the bonding interfaces between the AZ31 and Mg-0.6Gd regions near the edges ($r \approx 4$ mm) of the HPT-processed discs for *N* = 1/2, 10 and 20 turns in the two modes of secondary electron mode (SE) and BSE. Samples for SEM analysis were prepared using an Hitachi IM4000 ion milling system to eliminate all deformation, stresses and oxide layers.

A detailed microstructural analysis for the sample processed to $N = 20$ turns was carried out using a transmission electron microscope (TEM-JEOL JEM 1200) operating at an accelerating voltage of 120 kV and a CS-corrected dedicated scanning transmission electron microscope (STEM-Hitachi HD2700) operating at 200 kV. The TEM/STEM observations were prepared using a Focused Ion Beam (FIB) Hitachi NB-5000 microscope. Lamellas were cut from the cross-sections of samples in the direction parallel to RD and the STEM observations were carried out in bright-field (BF) and high-angle annular dark field (HAADF) modes. For some samples, selected area electron diffraction (SAED) patterns were also obtained.

Vickers microhardness measurements were taken using a Mitutoyo HM-200 with a load of 50 gf and a dwell time of 10 s. The disc samples were cut vertically across the disk diameters and the cross-sections were polished to mirror-like surfaces. A series of hardness values were recorded on these vertical cross-sections, measuring $8000 \times 450\ \mu m^2$, where a rectilinear grid pattern, having 150 μm separation between adjacent points, was applied for the automated measurement procedure. The recorded hardness values gave a total of 248 points and these points were used for construction of color-coded contour maps.

3. Experimental results

3.1. Initial microstructures before HPT processing

Figure 2 shows the initial microstructures of (a) and (c) AZ31 and (b) and (d) the Mg-0.6Gd alloys taken by optical microscopy (upper row) and SEM in BSE mode (lower row).

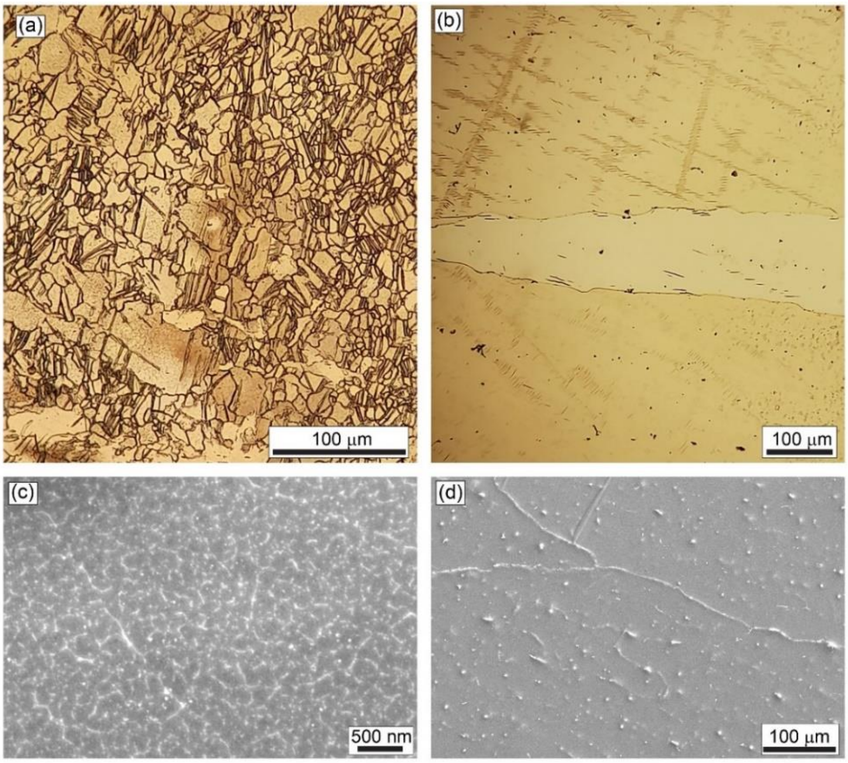

Figure 2: Initial microstructures of AZ31 on left and the Mg-0.6Gd alloy on right: (a, b) by optical microscopy and (c, d) by SEM in BSE mode.

In the initial state the AZ31 alloy exhibited a typical deformation microstructure having a mixture of elongated deformed grains and small recrystallized grains (Figure 2a) with a mean grain size of ~16 ±2.5 μm and the presence of a high fraction of twins. Figure 2c shows that the AZ31 alloy contained massive nano-sized particles that were homogenously distributed within the microstructure. By contrast, the Mg-0.6Gd alloy exhibited a typical as-cast microstructure with coarse grains (Figure 2b) and with the presence of metastable large particles that were distributed reasonably homogenously (Figure 2d).

3.2. Microstructure characterization using SEM and TEM after HPT processing

Figure 3 shows SEM images (upper row) of the AZ31/Mg-0.6Gd hybrid material after HPT processing for N = 1/4 turn near the centre, mid-radius and edge of the disc, where the estimated equivalent strains by eq. (1) are ~0.3, ~3.6 and ~6.5, respectively. The elemental compositions of the magnified zone from the mid-radius area (red frame) are determined through Mg, Al, Zn and Gd EDS elemental mapping (lower row). In addition, the chemical compositions of points marked 1-3 in this mid-radius area are given in Table 1. The total initial disc height of 1.7 mm decreased to ~0.63 mm after HPT processing and the AZ31 and Mg-0.6Gd alloys bonded successfully as shown in the centre of the disc.

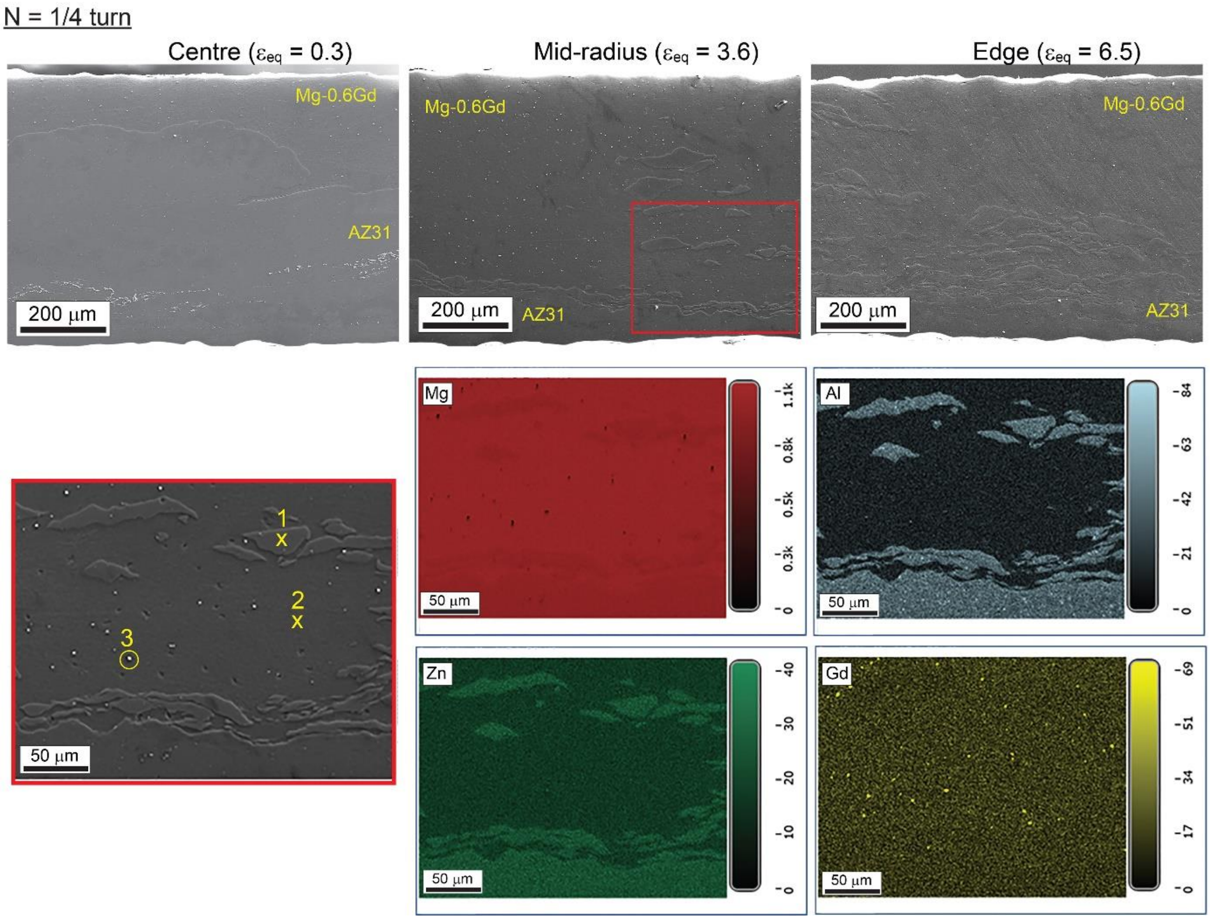

Figure 3: SEM images (upper row) of the AZ31/Mg-0.6Gd hybrid material after HPT processing for *N* = 1/4 turn near the centre, mid-radius and edge of the disk. EDS maps (lower rows) for the Mg, Al, Zn and Gd elements in the selected zone from the mid-radius region denoted by the red frame.

A fragmentation of the AZ31 alloy into layers occurred in the mid-radius area and the numbers of AZ31 layers increased near the edge of the sample. Such variations in morphology of the AZ31 layers are caused by the different strains introduced across the disc by the HPT processing since, as shown in eq. (1), the imposed strain varies from zero at the disc centre to a maximum at the edge. Table 1 indicates that the atomic percentage of Mg (89.5 %) and Gd (10.5 %) at point 3 suggests that this particle should be Mg_5Gd (83% of Mg and 17% of Gd, in at. %) second phase which is in good agreement with the binary Mg–Gd phase diagram [42] and reports in the literature [51-53].

Table 1. Chemical composition at different locations on the sample processed for *N* = 1/4 turn as shown in Figure 3.

	Point 1		Point 2		Point 3	
	wt. %	at. %	wt. %	at. %	wt. %	at. %
Mg	96.2	97.1	99.1	99.9	56.9	89.5
Gd	-	-	0.9	0.1	43.1	10.5
Al	2.7	2.5	-	-	-	-
Zn	0.6	0.2	-	-	-	-
Mn	0.5	0.2	-	-	-	-

Figure 4 presents SEM micrographs with different magnifications near the centre of the sample processed for *N* = 1/4 turn and at the edges for the samples processed for *N* = 1/2 and 10 turns where the equivalent strains for these three conditions are ~0.3, ~11.5 and ~230, respectively. The disc processed for *N* = 1/4 turn reveals an interesting microstructural evolution of the Mg-0.6Gd alloy. Thus, the microstructure is heterogenous through the thickness but near the interface, at about 26 µm of thickness, the microstructure is very refined. Far from the interface there are elongated large grains containing twins that are marked by arrows in the magnification of the red frame area. Shear bands are also present in this zone as indicated by the dashed white lines. Although the microstructure of the AZ31 region appears homogenous through the thickness, the magnification within the yellow frame in AZ31 shows that the microstructure is formed principally of a mixture of refined grains and deformed grains containing twins.

The microstructure of the Mg-0.6Gd alloy is homogenous through the thickness with increasing numbers of HPT turns as demonstrated at the edge of the disc processed for *N* = 1/2 turn. An EDS analysis was performed for this sample at four different positions labelled 1-4 and the recorded elemental compositions are listed in Table 2.

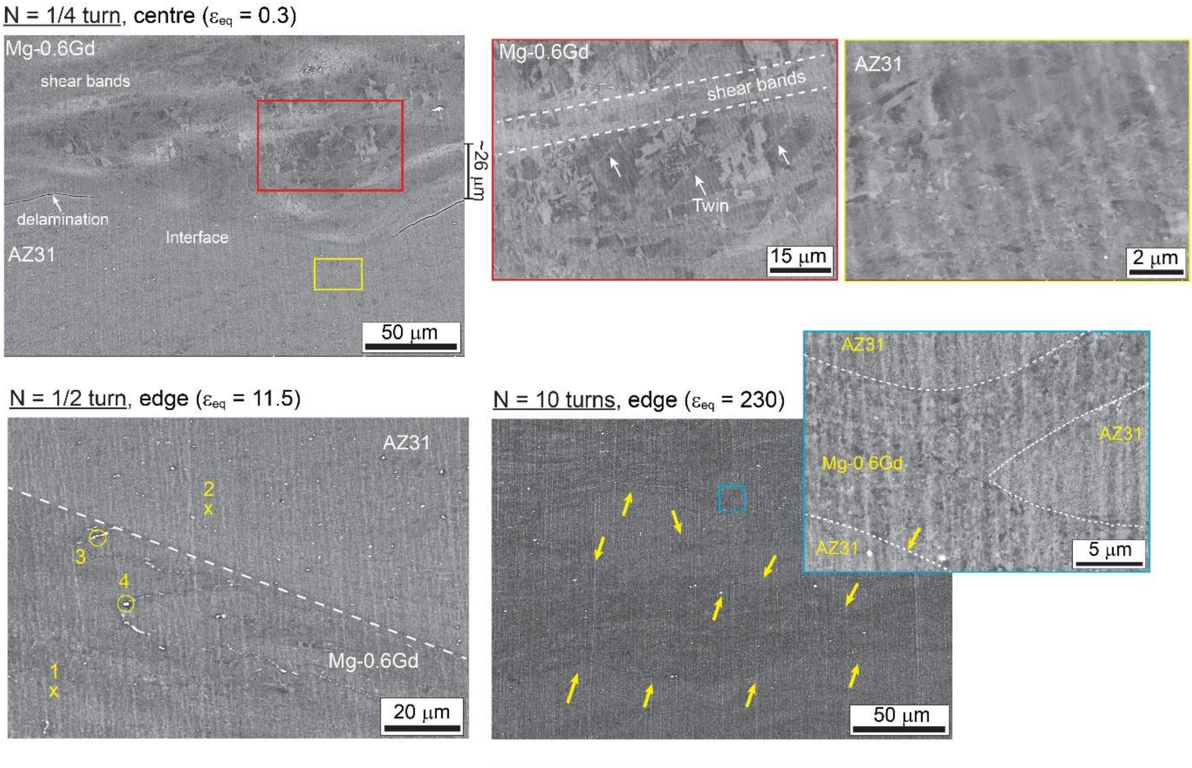

Figure 4: SEM micrographs with different magnifications near the centre of a sample processed for *N* = 1/4 turn and at the edge of samples processed for *N* = 1/2 and 10 turns, respectively. Red and yellow frames show magnifications of Mg-0.6Gd and AZ31 regions of sample processed for *N* = 1/4 turn, respectively. White arrows show the presence of a twin in Mg-0.6Gd region of sample processed for *N* = 1/4 turn. The dashed line shown in the sample processed for *N* = 1/2 turn presents the interface between the AZ31 and Mg-0.6Gd regions. Yellow arrows and the blue frame indicate the bending of the interfaces and the formation of multilayers in the sample processed for *N* = 10 turns.

In addition to the presence of Mg_5Gd second phase particles at point 3 in the Mg-0.6Gd region, new particles were detected at point 4 containing an exceptionally high fraction of Gd (93.1 %, wt.%) and these are probably associated with fragmentation of the initial Mg_5Gd second phase particles. The presence of Si element in point 3 is probably due to grinding with SiC papers during the sample preparation. A bending of the interfaces and the formation of multilayers is visible in the sample after 10 turns as indicated by the yellow arrows and the magnified region in the blue frame. Nevertheless, there was no evidence for any delamination between the layers and the two alloys bonded perfectly as shown by the magnified region in the blue frame.

Table 2. Chemical compositions at different locations on the sample processed to *N* = 1/2 turn as shown in Figure 4.

	Point 1		**Point 2**		**Point 3**		**Point 4**	
	wt. %	at. %	wt. %	at. %	wt. %	at. %	wt. %	at. %
Mg	100	100	95.2	96.1	54.5	85.2	6.9	32.5
Al	-	-	4.0	3.6	-	-	-	-
Zn	-	-	0.8	0.3	-	-	-	-
Gd	-	-	-	-	42.1	10.2	93.1	67.5
Si	-	-	-	-	3.4	4.6	-	-

A series of observations by TEM in BF and STEM in BF and HAADF modes are shown in Figures 5 and 6 with different magnifications for the AZ31/Mg-0.6Gd interface near the edge of the disc processed for *N* = 20 turns where the equivalent strain is ~460.

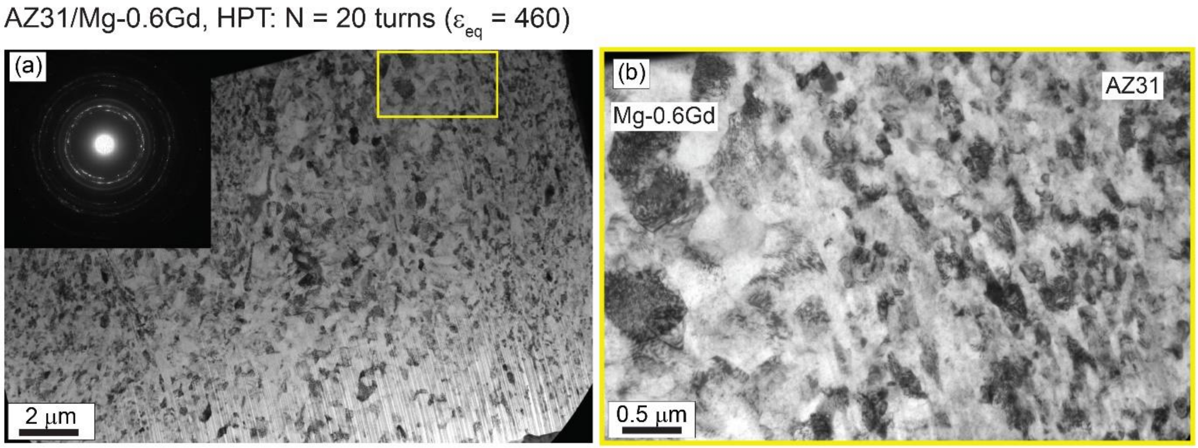

Figure 5: TEM-BF image near the edge of the disc processed for N = 20 turns at (a) low magnification with the corresponding SAED pattern and (b) in an enlargement of the area within the yellow frame shown in Figure 5a.

The microstructure shown in the low magnification TEM image and the continuous rings in the SAED pattern provide clear evidence for grain refinement with the development of HAGBs in the hybrid AZ31/Mg-0.6Gd system. A region near the formed interface between the AZ31 and Mg-0.6Gd alloy is shown in Figure 5b representing an enlargement of the area within the yellow frame in Figure 5a.

Figures 6a and 6b show another interface region in STEM-BF and HAADF modes, respectively, and the AZ31 regions at high magnification are shown in Figures 6c and 6d, respectively. These images demonstrate that the AZ31 alloy underwent greater grain refinement than the Mg-0.6Gd alloy. Thus, the AZ31 region shows reasonably equiaxed grains with a small average size of ~0.11±0.06 µm whereas the Mg-0.6Gd region exhibits an equiaxed microstructure with a larger average grain size of ~0.40±0.03 µm. The STEM-HAADF image shown in Figure 6b reveals a weak fraction of an Mg_5Gd phase marked by an arrow in the Mg-0.6Gd region and this contrasts with the presence of spherical particles with diameters in the range of ~10-24 nm homogenously distributed in the AZ31 region as can be seen in the STEM-HAADF image shown in Figure 6d. A Table of EDS results included in Figure 6e identifies these particles as the $Mg_{17}Al_{12}$ phase and some of these particles also contain Zn. There is no evidence for the formation of any new intermetallic phases within the examined regions of this hybrid AZ31–Mg-0.6Gd system.

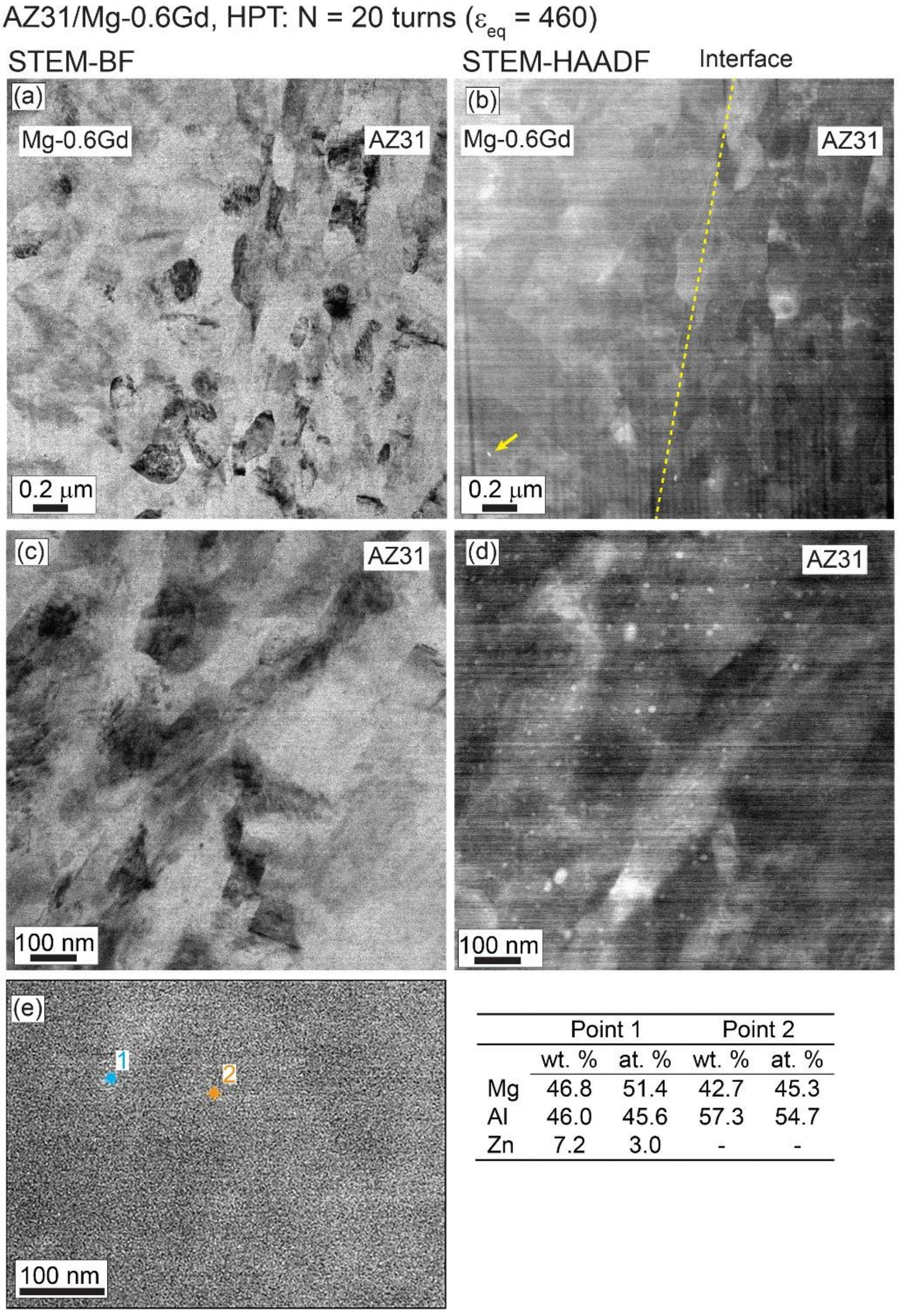

	Point 1		Point 2	
	wt. %	at. %	wt. %	at. %
Mg	46.8	51.4	42.7	45.3
Al	46.0	45.6	57.3	54.7
Zn	7.2	3.0	-	-

Figure 6: STEM images in (a) BF and (b) HAADF at low magnification near the edge of the disc processed for *N* = 20 turns, high magnification STEM images in (c) BF and (d) HAADF showing AZ31 regions and (e) EDS analysis of particles present at points 1 and 2 in the AZ31 region. Yellow dashed line in Figure 6b shows the interface between the AZ31 and Mg-0.6Gd regions.

3.3. Microstructure and texture evolution from EBSD

3.3.1. Microstructure evolution near the interfaces after HPT processing

Figures 7 and 8 show the orientation imaging micrographs (OIM) in inverse pole figure (RD-IPF) maps and grain size distributions, respectively, at the AZ31/Mg-0.6Gd interfaces near the centres, mid-radii and edges of samples processed for (a) 1/4, (b) 1/2, (c) 5, (d) 10 and (e) 20 turns.

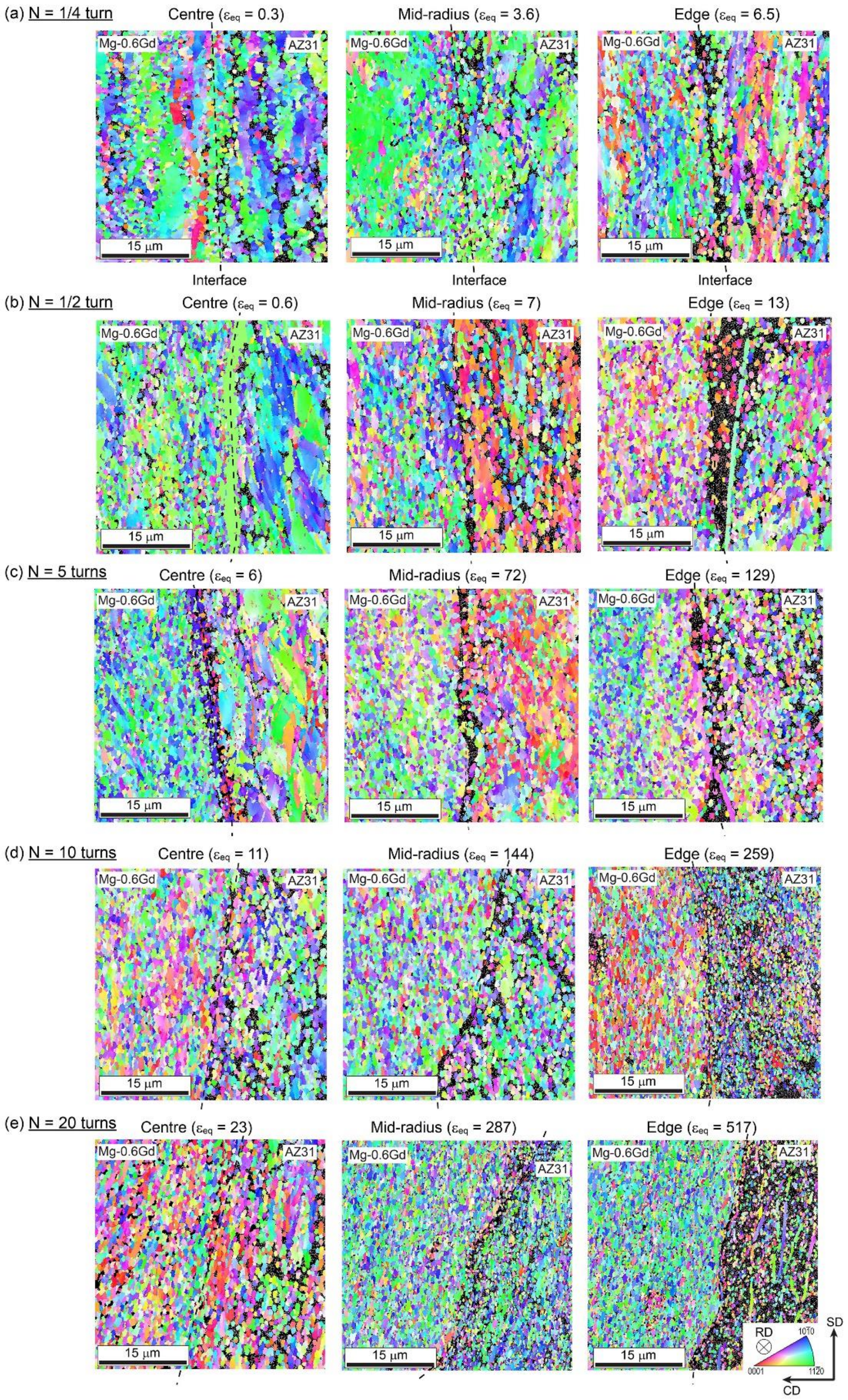

Figure 7: RD-IPF maps at the interface near the centre, mid-radius and edge of samples processed for (a) 1/4, (b) 1/2, (c) 5, (d) 10 and (e) 20 turns. The interface between the AZ31 ang Mg-0.6Gd regions is marked by a dashed black line in each RD-IPF map.

The AZ31 and Mg-0.6Gd regions are indicated in the RD-IPF maps and the interface in each area is marked by a dashed black line in Figure 7 where RD is perpendicular in each OIM. The mean grain sizes at the interfaces in each measurement are depicted in the grain size distribution plots in Figure 8.

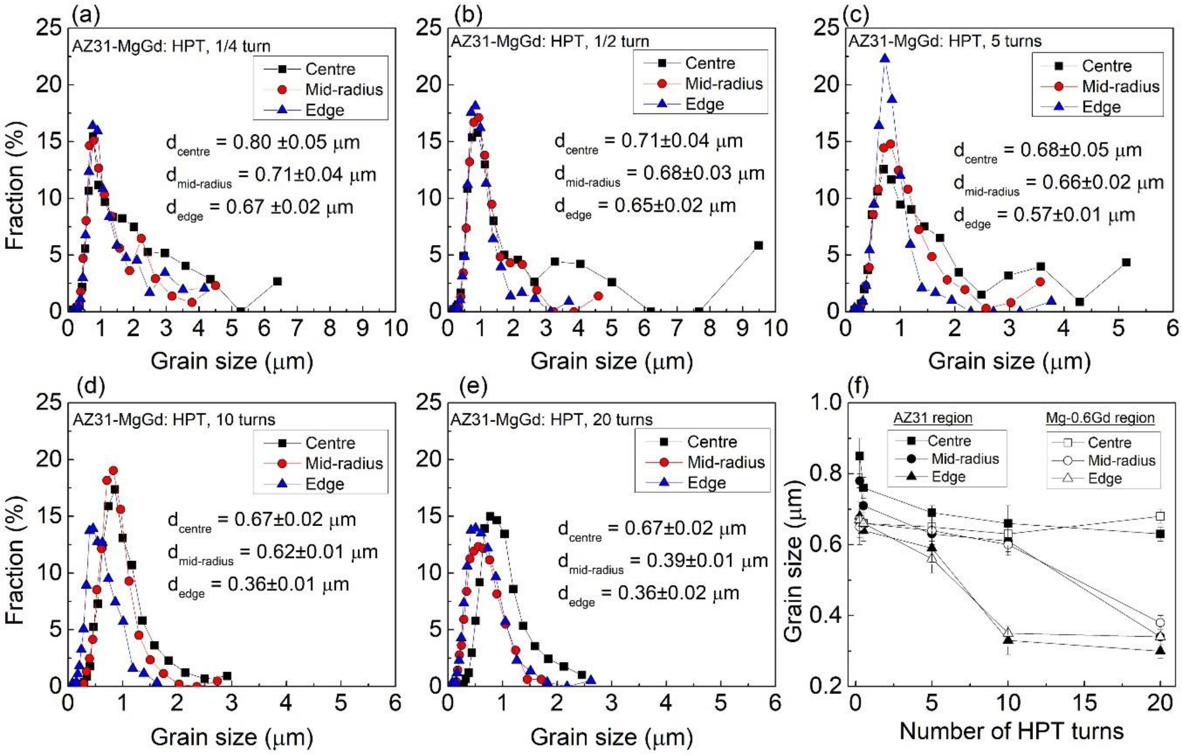

Figure 8: Grain size distributions at the interface near the centre, mid-radius and edge of samples processed for (a) 1/4, (b) 1/2, (c) 5, (d) 10 and (e) 20 turns and (f) evolution of the mean grain size in the AZ31 and Mg-0.6Gd regions as a function of numbers of HPT turns.

The RD-IPF maps in Figure 7 show the presence of black zones especially in the AZ31 region where these are due to the high amounts of deformation in the sample. The grain size distributions appear bimodal at the lower numbers of HPT rotations in the range of ~1/4-5 turns where a group of grains of <1 µm is present with another group of grains having an average size of ~3 µm or larger. With further HPT processing, the distribution of grain sizes becomes more uniform with an average value of less than 1 µm throughout the disc diameter.

These quantitative measurements show there is excellent grain refinement to an average of ~0.80±0.05 µm near the centre of the sample after 1/4 turn and thereafter the mean grain size appears to saturate at ~0.67±0.02 µm after 10 turns. There is a net decrease to about ~0.36±0.02 µm at the edge of the sample after 10 turns and a similar grain size is evident at the mid-radius position after 20 turns.

The evolution of the mean grain size corresponding to the AZ31 and Mg-0.6Gd regions is shown in Figure 8f as a function of the numbers of HPT turns. These curves indicate that the average grain sizes of both alloys decrease slowly near the centres of the discs and more rapidly near the mid-radius and edge positions due to the larger imposed strains. At higher numbers of HPT turns, the average grain size in the AZ31 region is slightly lower than in the Mg-0.6Gd region and the final values after 20 turns at the edges of the discs are ~0.30±0.02 and ~0.34±0.02 µm, respectively.

Figure 9 shows the fractions of separate grain boundary types for very low grain boundaries (VLAGBs) with misorientations of $2° < \theta < 5°$, LAGBs with $5° < \theta < 15°$ and HAGBs with misorientations $\theta > 15°$ at the interfaces near the centre, mid-radius and edge of samples processed for (a) 1/4, (b) 1/2, (c) 5, (d) 10 and (e) 20 turns. In addition, the evolution of the HAGBs fraction of the AZ31 and Mg-0.6Gd regions is shown in Figure 9f as a function of the numbers of HPT turns. In general, the fractions of VLAGBs, LAGBs and HAGBs are similar through the distance from the centre of each disc. It is apparent that the fraction of VLAGBs decreases with increasing numbers of HPT turns up to 5 turns and then saturates at ~18 % whereas the fraction of HAGBs increases due to the occurrence of DRX and reaches a value of ~75% after 20 turns. There are low fractions of LAGBs of the order of ~10% after any number of HPT turns.

Figure 9f shows that the fraction of HAGBs increases with increasing numbers of HPT turns up to 5 turns for both alloys and then saturates at each position. In addition, the HAGBs fraction for the Mg-0.6Gd region is higher at ~80% than for the AZ31 region at ~65% and this confirms the occurrence of a higher fraction of DRX in the Mg-0.6Gd alloy.

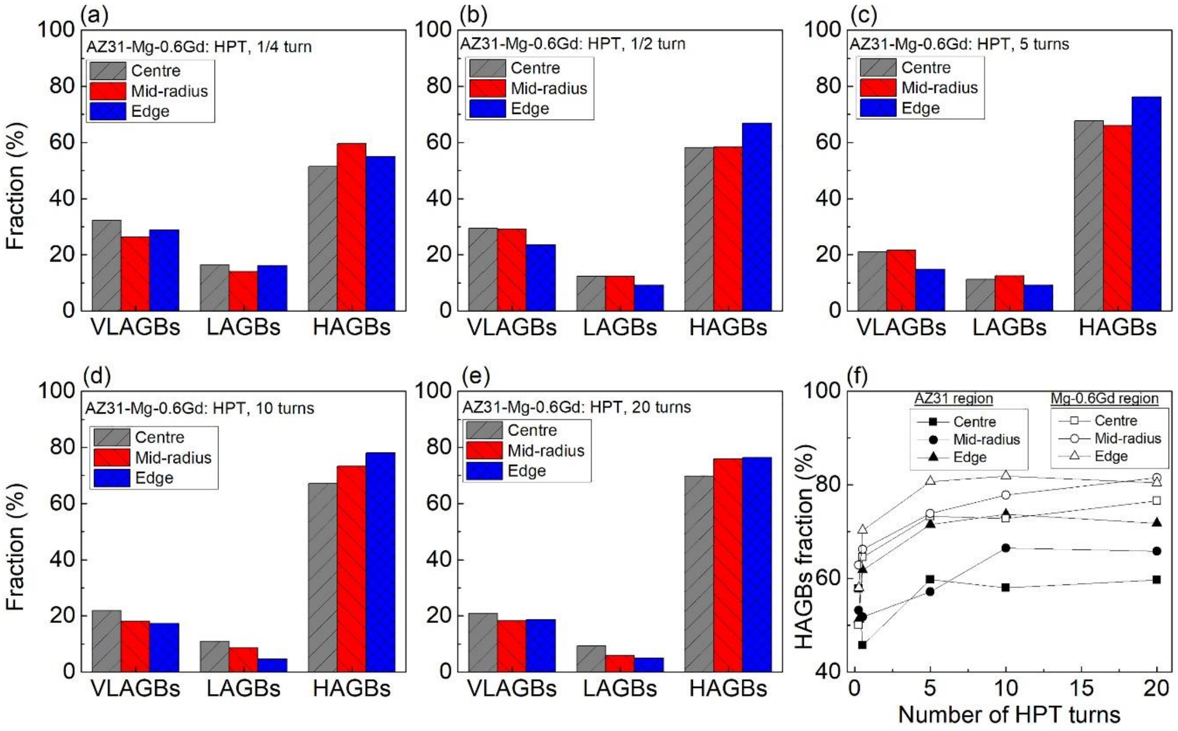

Figure 9: Fraction of VLAGBs, LAGBs and HAGBs at the interface near the centre, mid-radius and edge of samples processed for 1/4, 1/2, 5, 10 and 20 turns, and (f) evolution of the HAGB fraction of the AZ31 and Mg-0.6Gd regions as a function of numbers of HPT turns.

Noticeable microstructural features were extracted from the RD-IPF maps near the centres of the discs after (a) 1/2 turn and (b) 5 turns in Figure 10. In practice, the AZ31 and Mg-0.6Gd alloys exhibit different deformation features and mechanisms. As observed in Figure 10a, the GOS map shows that 28% of the Mg-0.6Gd grains are dynamically recrystallized and ultra-fine equiaxed grains are formed at the interface after ε_{eq} = 0.6 where this microstructural feature is readily visible within the marked oval in the RD-IPF map. Typical elongated deformed grains develop in the AZ31 region and the DRX is limited to only ~10% by comparison with the Mg-0.6Gd region. A magnification of the area within the red frame in the AZ31 region after 1/2 turn shows that these grains host different twin types.

(a) N = 1/2 turn: centre (ε_{eq} = 0.6)

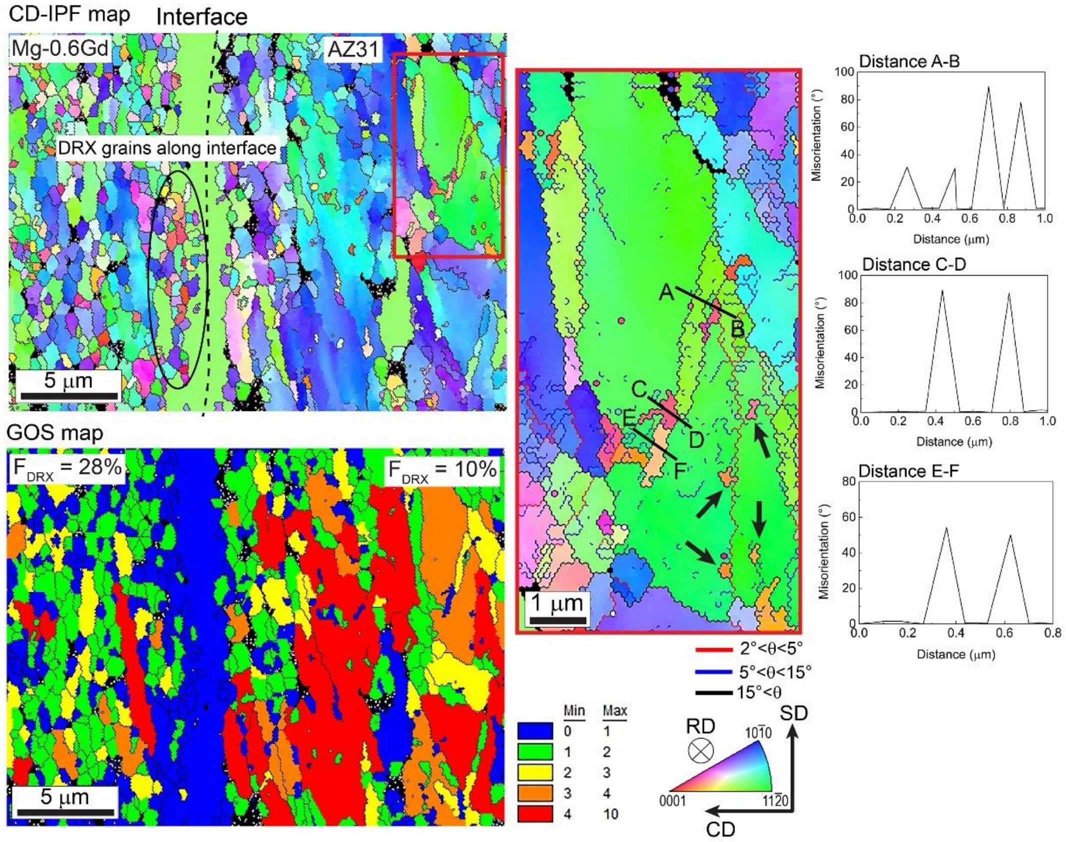

(b) N = 5 turns: centre (ε_{eq} = 6)

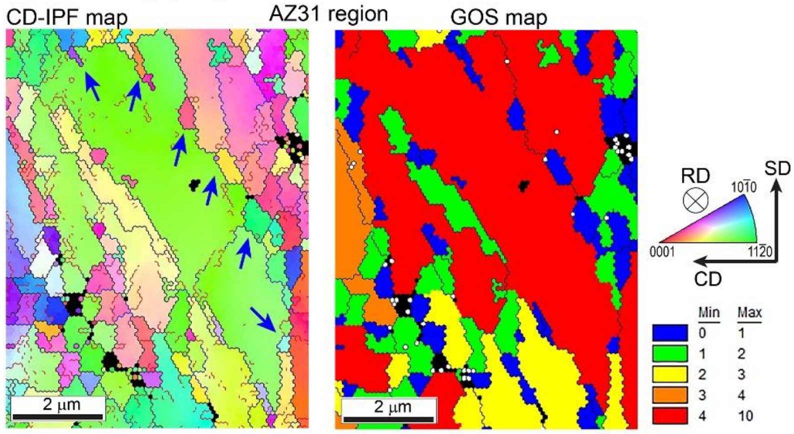

Figure 10: (a) RD-IPF and GOS maps and misorientation profiles corresponding to the lines A-B, C-D and E-F in the red frame near the centre of the disc processed for 1/2 turn and (b) RD-IPF and GOS maps showing the occurrence of the SIBM mechanism in the AZ31 region in the centre of the disc processed for 5 turns. The black circle in the Mg-0.6Gd region of the sample processed for 1/2 turn indicates the formation of DRX grains along the interface. The magnified red frame in the AZ31 region after 1/2 turn shows the presence of different twin types. The black arrows in the red frame show the occurrence of the SGD mechanism. The blue arrows indicate the occurrence of the SIBM mechanism.

The misorientation profiles at the distances of AB, CD, and EF gives evidence for the presence of double twins 22°<11-20>, extension twins 86° <11-20> and contraction twins 56°<11-20>, respectively. These twins contain LAGBs which suggest the possibility of the formation of new finer grains with further deformation. This mechanism corresponds to the traditional twin-induced dynamic recrystallization (TDRX) [54].

There is also another DRX mechanism within the AZ31 grains in the same magnified RD-IPF map where fine grains are formed within the deformed grain, as marked by black arrows, by the sub-grain development (SGD) mechanism [55]. In this mechanism, high densities of dislocations within the deformed grains lead to the development of sub-grains boundaries which transform to LAGBs and ultimately to new refined grains with HAGBs. In addition, the RD-IPF and GOS maps of the AZ31 region in the centre of the disc processed for 5 turns, as shown in Figure 10b, reveals the formation of dynamically recrystallized grains marked with blue arrows along the grain boundaries and this indicates the occurrence of the strain-induced boundary migration (SIBM) mechanism [14].

3.3.2. Texture evolution at the interfaces

The texture evolution at the interface near the centre, mid-radius and edge of the samples processed for 1/4, 1/2, 5, 10 and 20 turns is given in Figure 11 using recalculated {0002} pole figures. The positions of the ideal shear texture components in the {0002} pole figures projected in the SD-RD plane for materials with an HCP structure are shown for comparison in Figure 11 and their description in the form of the Euler angles (φ_1, Φ, φ_2) is given in Table 3.

Table 3. Position of ideal shear texture components for HCP materials and alloys projected in the SD-RD planes [16].

Notation	B-fiber	P-fiber	Y-fiber	C_1-fiber	C_2-fiber
(φ_1, Φ, φ_2)	(0-60, 0, 0)	(180, 0-90, 30)	(180, 60, 0-60)	(90, 60, 0-60)	(270, 60, 0-60)

(a) N = 1/4 turn

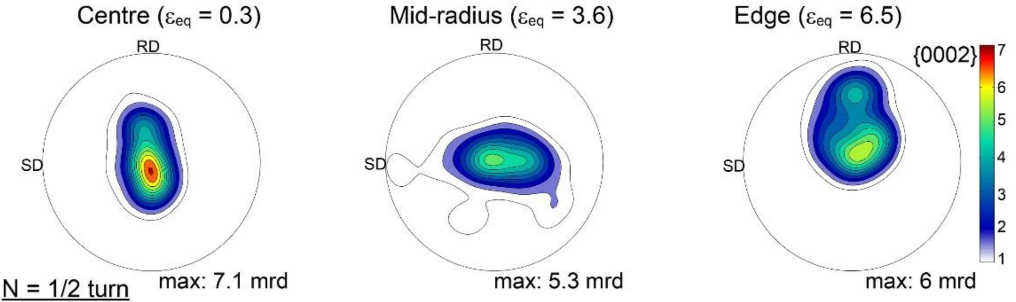

(b) N = 1/2 turn

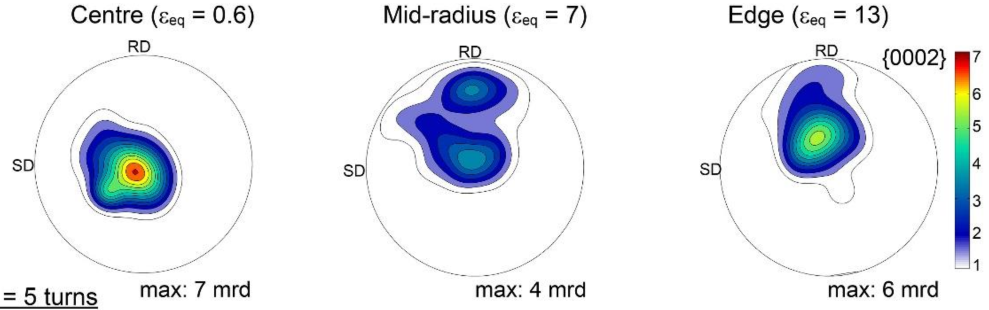

(c) N = 5 turns

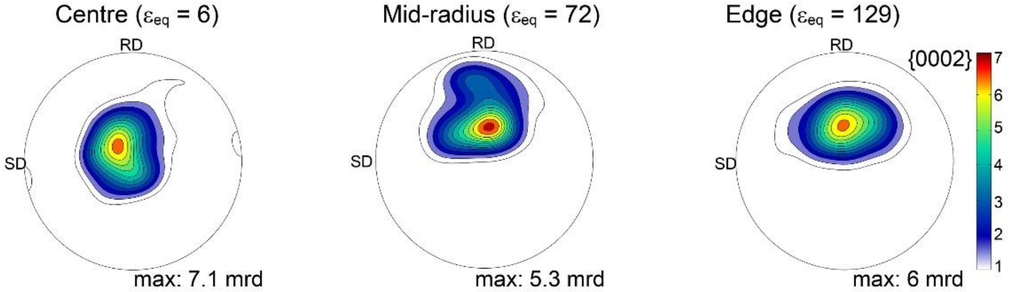

(d) N = 10 turns

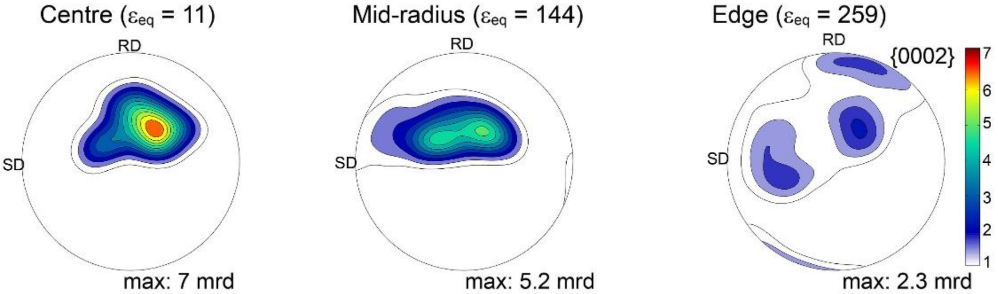

(e) N = 20 turns

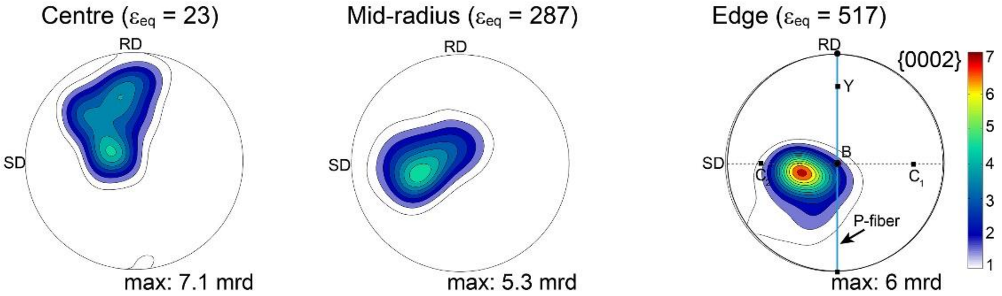

Figure 11: Recalculated {0002} pole figures at the interface near the centre, mid-radius and edge of samples processed for (a) 1/4, (b) 1/2, (c) 5, (d) 10 and (e) 20 turns.

It is apparent that the texture is heterogeneously distributed through the diameters of all of the examined discs. At the centres of the discs, a typical basal texture (B-fiber) is developed through 10 turns and then Y-fibers with B-fibers are formed in the centres of samples processed for 20 turns. At the mid-radius of the discs, the B-fiber rapidly transforms to B with Y-fibers after processing for 1/2 turn and then changes to a new fiber where the B-fiber deviates by about 20° towards RD after 10 turns. Thereafter, it changes again to a C_2-fiber through 20 turns. At the edges of the discs, the B and Y fibers are formed rapidly after processing for 1/4 turn and this changes to a deviated B-fiber after processing through 5 turns and thereafter gradually changes to a C_2-fiber through 20 turns. Consequently, the texture formation evolves through 4 stages as a function of the equivalent strain. These stages may be designated as stage 1 ($0.3 < \varepsilon_{eq} < 6.5$) with the presence of a basal texture; stage 2 ($6.5 < \varepsilon_{eq} < 72$) where a Y-fiber is formed with a B-fiber; stage 3 ($129 < \varepsilon_{eq} < 259$) where the Y-fiber disappears and the B-fiber deviates by about 20° towards RD; and stage 4 ($259 < \varepsilon_{eq} < 517$) where the C_2-fiber develops.

Figure 12 presents the separate texture evolution in the AZ31 and Mg-0.6Gd regions in terms of the recalculated {0002} pole figures through the 4 stages of texture evolution. It is important to note that the as-received AZ31 alloy exhibited a typical basal texture (B-fiber) as described in an earlier report [56] while the initial texture of the as-cast Mg-0.6Gd alloy was not measured since the alloy contained limited grain numbers and multiple coarse grains as shown in Figure 2. The texture of the AZ31 alloy changes significantly through these four stages similar to the behaviour of the texture around the interfaces as shown in Figure 11. The B-fiber changes to a B-fiber with Y-fiber during stages 1 and 2, the texture changes continuously through stage 3 and finally a C_2-fiber with a weak C_1-fiber develops in stage 4. By contrast, the basal texture formed in the Mg-0.6Gd alloy at stage 1 seems quite stable through the 4 stages except for a deviation from its ideal position.

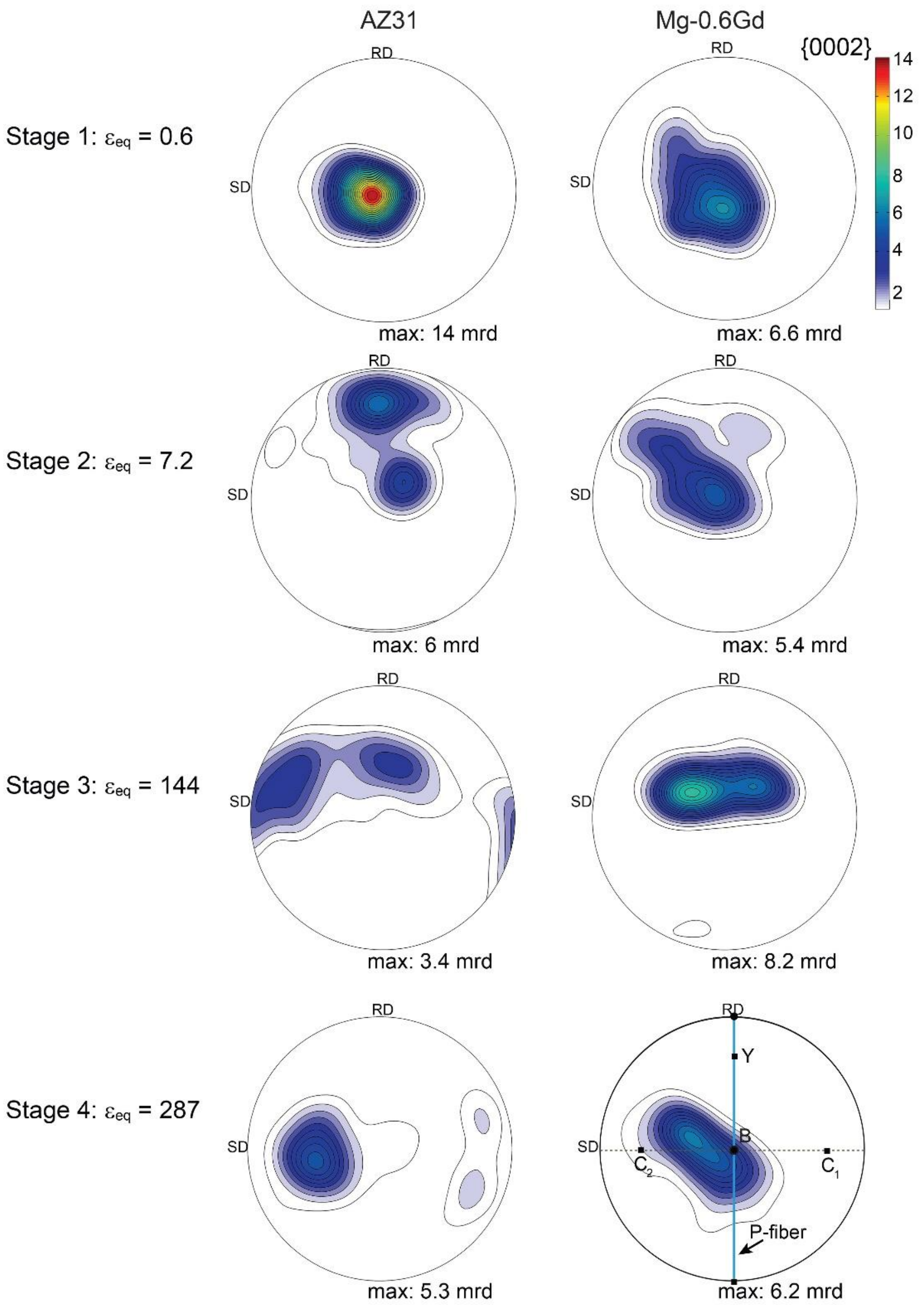

Figure 12: Evolution of recalculated {0002} pole figures corresponding to the AZ31 and Mg-0.6Gd regions in stages 1 ($\varepsilon_{eq} = 0.6$), 2 ($\varepsilon_{eq} = 7.2$), 3 ($\varepsilon_{eq} = 144$) and 4 ($\varepsilon_{eq} = 287$).

3.4. Microhardness evolution after HPT processing

Figure 13 shows the color-coded maps depicting the distributions of microhardness over the radial cross-sections of the HPT-processed hybrid system for 1/4, 1/2, 5, 10 and 20 turns. The initial microhardness values of the as-received AZ31 and Mg-0.6Gd alloys were ~72.5 and

~24.5 Hv, respectively. The evolution of microhardness as a function of numbers of HPT turns was reported earlier for AZ31 alloys to lie in the range of Hv ≈ 60–120 [4, 10]. There are no reports of the microhardness of the Mg-0.6Gd alloy after HPT processing but it is reasonable to anticipate the Hv range is probably close to ~30–50 as reported for an HPT-processed Mg-0.4Dy (wt.%) alloy [7] and ~35–65 reported for a Mg-0.6Ce (wt.%) alloy processed by equal-channel angular pressing (ECAP) [57].

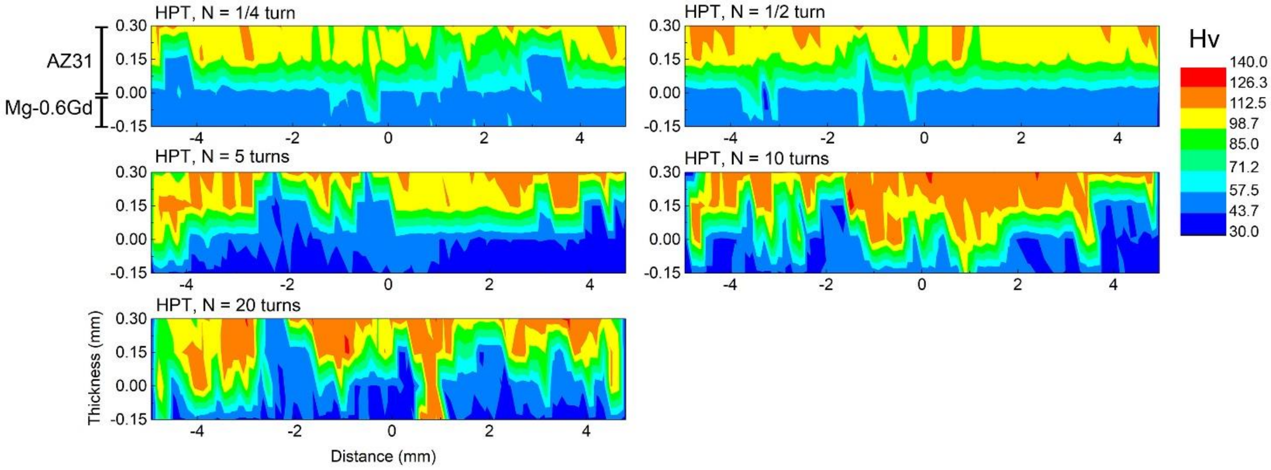

Figure 13: Color-coded microhardness maps of the hybrid AZ31/Mg-0.6Gd material processed by HPT for 1/4, 1/2, 5, 10 and 20 turns.

It is readily apparent from Figure 13 that the values of the microhardness increase with increasing numbers of HPT turns. The interface between the AZ31 and Mg-0.6Gd alloys are reasonably flat along the disc diameters 1/4 and 1/2 turn but after 10 turns there is a heterogeneously distributed microhardness demonstrating a bending of the interface and the consequent formation of multilayers as observed in the SEM image. Thereafter, the microhardness distributions tend to saturate at values of ~40 and ~125 Hv for the Mg-0.6Gd and AZ31 alloys, respectively.

The shifting of the bonding interfaces and the development of multilayers of the AZ31/Mg-0.6Gd hybrid material can be easily highlighted by plotting the evolution of microhardness along the diameter in the mid-thickness of the HPT-processed disc as shown in Figure 14. The average microhardness of the Mg-0.6Gd alloy increases from ~24.5 Hv in the as-received condition to ~54.5 Hv after 1/4 turn and then decreases and saturates at ~44.5 Hv after 5 turns. Up to 5 turns, the microhardness shows values above 80 Hv in various positions along the disc diameter and this is attributed to the AZ31 alloy. Hence, it appears that within the mid-thickness there are discrete AZ31 layers in which the microhardness of the AZ31 alloy evolves from the as-received condition of ~72.5 Hv to values close to ~125 Hv after 10 and 20 turns.

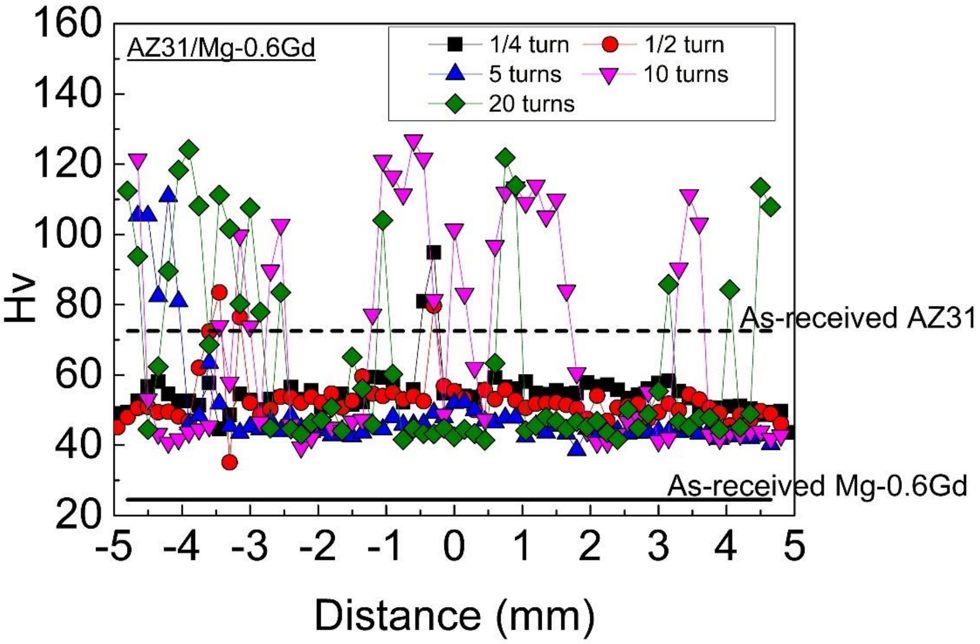

Figure 14: Evolution of microhardness along the diameter in the mid-thickness of the AZ31/Mg-0.6Gd discs after HPT processing for 1/4, 1/2, 5, 10 and 20 turns. The continues and dashed black lines indicate the initial microhardness values of Mg-0.6Gd and AZ31 alloys, respectively.

4. Discussion

This report describes the first characterization of a dissimilar Mg-based hybrid material fabricated by HPT processing at RT using initial discs of two different Mg alloys where detailed microstructural observations of the AZ31/Mg-0.6Gd hybrid material provide confirmation that HPT processing is an effective technique for the bonding of Mg-based alloys. The mechanism of the grain refinement and the nature of the texture development in the AZ31/Mg-0.6Gd hybrid material are now discussed.

4.1. Grain refinement mechanisms

Figure 15 shows (a) the evolution of the mean grain sizes and the HAGBs fractions at the interfaces, (b) the mean grain sizes, (c) the fractions of HAGBs in the separate AZ31 and Mg-0.6Gd regions recorded from the EBSD measurements and (d) the microhardness values taken at the mid-thickness of the discs re-plotted as a function of the equivalent strain. The evolution of mean grain size and HAGBs at the interfaces and for the AZ31 region are readily separated into four separate stages which match the texture evolution described in section 3.3.2. In stage 1 at $0.3 < \varepsilon_{eq} < 6.5$ the grain size decreases and the fraction of HAGBs increases slowly, in stage 2 at $6.5 < \varepsilon_{eq} < 72$ the grain size and fraction of HAGBs are stable, in stage 3 at $72 < \varepsilon_{eq} < 259$ the grain size deceases and the fraction of HAGBs increases rapidly, and then in stage 4 at $259 < \varepsilon_{eq} < 517$ the grain size and the fraction of HAGBs appear reasonably stable based on the limited available data. Figure 15b shows that the mean grain size of the Mg-0.6Gd region was stable during the first and second stages and then decreases and stabilizes during the third and fourth stages, respectively. By contrast, the mean grain size of the AZ31 region was higher than for the Mg-0.6Gd region during the first stage, it was essentially equal to the Mg-0.6Gd region in stages 2 and 3 and then was slightly lower than for the Mg-0.6Gd alloy in stage 4. It is apparent from inspection of Figure 15c that the evolutions of the HAGBs fractions are generally similar for both the Mg-0.6Gd and AZ31 regions.

The stabilization of a mean grain size and the evolution of microhardness in stages 1 and 2 is evidence for a rapid softening with recovery behaviour in the Mg-0.6Gd alloy. Such behaviour was reported for a Mg-0.4Dy (wt.%) alloy during HPT processing [7]. The high microhardness values in stage 3 as in Figure 15d demonstrate the presence of the AZ31 alloy in the mid-thickness of the disc in the form of multilayers which coincide with the decrease in the mean grain size in Figure 15b.

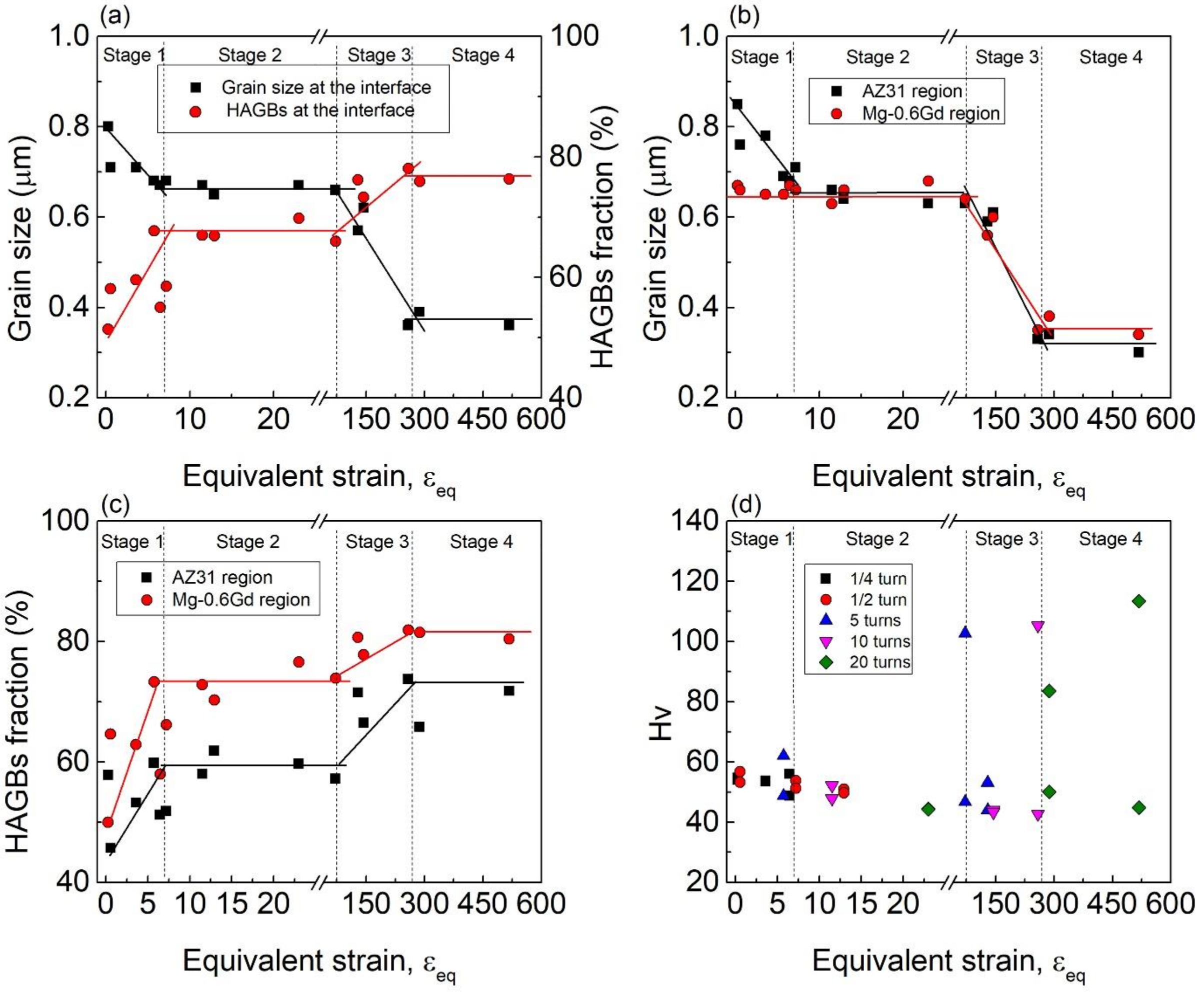

Figure 15: Evolution of (a) mean grain size and HAGBs fraction at the interfaces, (b) mean grain size and (c) HAGBs fractions of the AZ31 and Mg-0.6Gd regions obtained from EBSD measurements and (d) microhardness values taken from the mid-thickness of the HPT-processed discs as a function of the equivalent strain. Stage 1: $0.3 < \varepsilon_{eq} < 6.5$, stage 2: $6.5 < \varepsilon_{eq} < 72$, stage 3: $72 < \varepsilon_{eq} < 259$, and stage 4: $259 < \varepsilon_{eq} < 517$.

This result demonstrates that the effective strain must be larger than predicted by eq. 1 when the multilayers are developed which leads to extra grain refinement and texture modification in stages 3 and 4. Hence it is concluded that the occurrence of the first grain refinement in stages 1 and 2 (ε_{eq} ~0.3–72) is due to the strain induced by HPT processing and the second grain refinement in stages 3 and 4 (ε_{eq} ~72–517) is due to the development of multilayers as evident from the SEM images at the edge of the disc processed for 10 turns in Figure 4.

It is interesting to note that the formation of multilayers is still not homogenously distributed through the cross section of the disc even after a high number of HPT turns like 20 turns (ε_{eq} up to 517) as demonstrated by the non-homogenous distribution of microhardness shown in Figure 13. This observation indicates that more strain is probably needed for the fragmentation of AZ31 and Mg-0.6Gd alloys into thinner layers.

The microstructural observations obtained from EBSD, SEM and TEM indicate that the AZ31 and Mg-0.6Gd alloys have different grain refinement mechanisms. Thus, the mean grain size of ~0.11±0.06 µm obtained by TEM and STEM observations of the AZ31 alloy after HPT processing for 20 turns is smaller than the mean grain size of ~0.4±0.03 µm for the Mg-0.6Gd alloy. It follows from Figure 15c that the second grain refinement in stage 3 is stronger in the AZ31 alloy and this difference may be associated with the role of the alloying elements in the two materials (Al and Zn versus Gd) and the initial conditions of both alloys.

Figure 10 shows a clear example where the AZ31 and Mg-0.6Gd alloys behave differently at the interfaces during low strains. The TDRX and SGD mechanisms were detected in the AZ31 region after processing for $\varepsilon_{eq} = 0.3$. In addition, the SIBM mechanism was evident in the AZ31 region for a sample processed for $\varepsilon_{eq} = 6$ as shown in Figure 10b. Up to this strain, the microstructures of the AZ31 and Mg-0.6Gd regions were similar with the formation of equiaxed fine grains. However, even with the initial coarse grains of the Mg-0.6Gd alloy, it was not feasible to identify the grain refinement mechanisms near the interfaces since a homogenous ultrafine microstructure was rapidly developed at $\varepsilon_{eq} = 0.3$ as shown in Figure 7.

Nevertheless, Figure 4 reveals that the microstructure of the Mg-0.6Gd alloy far from the interface contains a combination of both twins and shear bands. These shear bands are reasonably homogeneously distributed within the microstructure where this is known as a characteristic of SPD Mg-RE alloys due to the effect of the RE elements and the easy activation of the <c + a> pyramidal slip system [58-60]. Consequently, it is concluded that the grain refinement mechanisms in the Mg-0.6Gd alloy is also controlled by twinning and slip deformation.

It is important to note that the Mg-0.6Gd alloy was more sensitive to the formation of ultrafine grain at the interface than the AZ31 alloy. This difference is attributed to the initial grain sizes of both alloys. As shown in Figure 2, the AZ31 alloy exhibits a microstructure with very small grains compared to the coarser grains that are initially present in the Mg-0.6Gd alloy. This is consistent with a proposed model where there is a critical initial grain size that is sufficiently small to ensure a homogeneous microstructure during deformation processing [13].

Although the grain refinement was rapid for the Mg-0.6Gd alloy near the interface, the AZ31 alloy exhibits an overall finer mean grain size after HPT processing as shown by TEM and STEM observations in Figures 5 and 6 and this is probably associated with the presence of second phase particles in the AZ31 alloy. Thus, the $Mg_{17}Al_{12}$ phase is present in the as-received alloy and this phase remains qualitatively present throughout the HPT processing. By contrast, HPT processing leads to a dissolution of the metastable phases present in the as-cast Mg-0.6Gd alloy and in this case the $Mg_{17}Al_{12}$ phase produces a strong pinning effect on grain boundary migration which delays the occurrence of DRX by suppressing the growth of the DRX grains.

Except only for the presence of the $Mg_{17}Al_{12}$ phase in the AZ31 alloy and the dissolution of the metastable phases in the Mg-0.6Gd alloy, there is no evidence for the formation of any new second phases in the AZ31/Mg-0.6Gd hybrid during HPT processing. An absence of formation of any intermetallic phases was reported earlier in a Mg/Al composite fabricated by HPT processing at RT while an additional heat treatment at 573 K for 1 h led to the formation of Al_3Mg_2 and $Al_{12}Mg_{17}$ phases since, it was suggested, processing at RT hinders the nucleation and growth of any second phase [61]. This suggests that it would be beneficial to investigate the microstructural evolution of the AZ31/Mg-0.6Gd hybrid material after a heat treatment.

4.2. Texture evolution during HPT processing

The basal texture (B-fiber) in HCP materials is often formed in the earlier stage of HPT processing and is maintained throughout the entire deformation processing [16]. The formation of the B-fiber causes a low formability of the material and hence it generally restricts the potential structural applications. The present results show that the texture evolution of the AZ31/Mg-0.6Gd hybrid material changes in Figure 11 as a function of equivalent strain and this provides an opportunity to design a new generation of Mg-based alloys having superior formability. This change in the texture evolution is connected directly with the change in grain refinement and deformation mechanisms [16] since the AZ31 and Mg-0.6Gd alloys undergo different grain refinement mechanisms and this affects the texture evolution of each alloy as shown in Figure 12.

Inspection of Figure 12 shows that the texture of the AZ31 alloy changes through the four stages whereas the basal texture of the Mg-0.6Gd alloy is retained through these stages except only for the deviation from its ideal position. The deviation of the B-fiber and its saturation through HPT processing was reported earlier in Mg-RE binary alloys [7, 62]. In accordance with the microstructural evolution of the AZ31 alloy, and by comparison with the Mg-0.6Gd alloy, the formation of the Y-fiber in the AZ31 alloy may be due to the presence of twins in the AZ31 sample after processing for 1/2 and 5 turns, and this is especially associated with the contraction and extension twins which produce a rotation of about 56° and 86° of the initial basal texture, respectively. A similar texture of B and Y-fibers was reported for the AZ31 alloy after processing by HPT at RT for 1 and 5 turns [63] and it was also reported that the development of the C_2-fiber is due to an activation of the pyramidal <c+a> slip system [64]. It is reasonable to conclude that the extra strain introduced by the bending and development of multilayers in the hybrid material facilitates the activation of the pyramidal <c+a> slip system in the AZ31 alloy. Nevertheless, further investigations are now needed to more fully explore the effect of the resultant texture on the formability of this new AZ31/Mg-0.6Gd hybrid material.

The present report demonstrates the possibility of joining dissimilar Mg-based alloys with HPT processing. Much research and investigation are now needed to explore the anisotropy of the mechanical properties across the disc and the thermal stability of the hybrid material. The results obtained will be useful for finding potential applications for this new hybrid material.

5. Summary and conclusions

- HPT processing at RT was successfully used to fabricate a dissimilar magnesium AZ31/Mg-0.6Gd hybrid material.
- The fabricated hybrid alloy exhibited two stages of grain refinements. The first grain refinement occurred during $\varepsilon_{eq} \approx 0.3$–72 due to the strain introduced by HPT processing and the second grain refinement was observed during $\varepsilon_{eq} \approx 72$–517 due to the extra strain induced from bending and the development of multilayers.
- The microstructure exhibited excellent grain refinement after 20 turns but the AZ31 region gave a greater grain size reduction (~0.11 ±0.06 µm) than the Mg-0.6Gd region (~0.40±0.03 µm).
- The grain refinement and DRX mechanisms in the AZ31 alloy were controlled by twinning, slip systems and the $Mg_{17}Al_{12}$ precipitates. The Mg-0.6Gd alloy showed rapid grain refinement but twinning and slip were the main mechanisms responsible for DRX.
- The texture of the AZ31 alloy changed from B-fiber to Y-fiber and C_2-fiber through HPT processing together with the formation of multilayers. The basal texture of the Mg-

0.6Gd alloy was stable through the HPT processing except for a deviation from its ideal position.

Acknowledgements

Dr-Ing. N. Hort and Dr. D. Letzig (MagIC, Germany) and Dr-Ing. Talal Al-Samman (RWTH-Aachen University, Germany) are gratefully acknowledged for providing the AZ31 and Mg-0.6Gd alloys, respectively. Two of the authors were supported by the European Research Council under Grant Agreement No. 267464-SPDMETALS (YH and TGL).

References

[1] K. Edalati, A. Bachmaier, V. A. Beloshenko, Y. Beygelzimer, V. D. Blank, W. J. Botta, K. Bryła, J. Čížek, S. Divinski, N. A. Enikeev, Y. Estrin, G. Faraji, R. B. Figueiredo, M. Fuji, T. Furuta, T. Grosdidier, J. Gubicza, A. Hohenwarter, Z. Horita, J. Huot, Y. Ikoma, M. Janeček, M. Kawasaki, P. Král, S. Kuramoto, T. G. Langdon, D. R. Leiva, V. I. Levitas, A. Mazilkin, M. Mito, H. Miyamoto, T. Nishizaki, R. Pippan, V. V. Popov, E. N. Popova, G. Purcek, O. Renk, Á. Révész, X. Sauvage, V. Sklenicka, W. Skrotzki, B. B. Straumal, S. Suwas, L. S. Toth, N. Tsuji, R. Z. Valiev, G. Wilde, M. J. Zehetbauer, X. Zhu, *Materials Research Letters* **2022**, 10, 163.

[2] Y. Huang, R. B. Figueiredo, T. Baudin, F. Brisset, T. G. Langdon, *Advanced Engineering Materials* **2012**, 14, 1018.

[3] A. Al-Zubaydi, R. B. Figueiredo, Y. Huang, T. G. Langdon, *Journal of Materials Science* **2013**, 48, 4661.

[4] J. Xu, X. Wang, M. Shirooyeh, G. Xing, D. Shan, B. Guo, T. G. Langdon, *Journal of Materials Science* **2015**, 50, 7424.

[5] A. S. J. Al-Zubaydi, A. P. Zhilyaev, S. C. Wang, P. Kucita, P. A. S. Reed, *Journal of Materials Science* **2016**, 51, 3380.

[6] R. B. Figueiredo, T. G. Langdon, *Advanced Engineering Materials* **2019**, 21, 1801039.

[7] A. Hanna, H. Azzeddine, R. Lachhab, T. Baudin, A.-L. Helbert, F. Brisset, Y. Huang, D. Bradai, T. G. Langdon, *Journal of Alloys and Compounds* **2019**, 778, 61.

[8] A. A. Khaleghi, F. Akbaripanah, M. Sabbaghian, K. Máthis, P. Minárik, J. Veselý, M. El-Tahawy, J. Gubicza, *Materials Science and Engineering: A* **2021**, 799, 140158.

[9] F. Meng, J. M. Rosalie, A. Singh, H. Somekawa, K. Tsuchiya, *Scripta Materialia* **2014**, 78-79, 57.

[10] J. Stráská, M. Janeček, J. Gubicza, T. Krajňák, E. Y. Yoon, H. S. Kim, *Materials Science and Engineering: A* **2015**, 625, 98.

[11] E. A. Lukyanova, N. S. Martynenko, V. N. Serebryany, A. N. Belyakov, L. L. Rokhlin, S. V. Dobatkin, Y. Z. Estrin, *Russian Metallurgy (Metally)* **2017**, 2017, 912.

[12] K. Bryła, J. Morgiel, M. Faryna, K. Edalati, Z. Horita, *Materials Letters* **2018**, 212, 323.

[13] R. B. Figueiredo, T. G. Langdon, *Journal of Materials Science* **2010**, 45, 4827.

[14] T. Sakai, A. Belyakov, R. Kaibyshev, H. Miura, J. J. Jonas, *Progress in Materials Science* **2014**, 60, 130.

[15] R. B. Figueiredo, S. Sabbaghianrad, T. G. Langdon, *IOP Conference Series: Materials Science and Engineering* **2017**, 194, 012039.

[16] H. Azzeddine, D. Bradai, T. Baudin, T. G. Langdon, *Progress in Materials Science* **2022**, 125, 100886.

[17] S. Tighiouaret, R. Lachhab, A. Hanna, H. Azzeddine, Y. Huang, T. Baudin, A.-L. Helbert, F. Brisset, D. Bradai, T. G. Langdon, *Advanced Engineering Materials* **2019**, 21, 1900801.

[18] Y. F. Sun, H. Fujii, T. Nakamura, N. Tsuji, D. Todaka, M. Umemoto, *Scripta Materialia* **2011**, 65, 489.

[19] M. Pouryazdan, B. J. P. Kaus, A. Rack, A. Ershov, H. Hahn, *Nature Communications* **2017**, 8, 1611.

[20] K. Oh-ishi, K. Edalati, H. S. Kim, K. Hono, Z. Horita, *Acta Materialia* **2013**, 61, 3482.

[21] J.-K. Han, K.-D. Liss, T. G. Langdon, M. Kawasaki, *Scientific Reports* **2019**, 9, 17186.

[22] J.-K. Han, K. Sugimoto, M. Kawasaki, K.-D. Liss, *Materials Letters* **2022**, 321, 132414.

[23] P. Bazarnik, A. Bartkowska, Y. Huang, K. Szlązak, B. Adamczyk-Cieślak, J. Sort, M. Lewandowska, T. G. Langdon, *Materials Science and Engineering: A* **2022**, 833, 142549.

[24] S. O. Rogachev, S. A. Nikulin, V. M. Khatkevich, N. Y. Tabachkova, R. V. Sundeev, *Russian Metallurgy (Metally)* **2018**, 2018, 372.

[25] D. Hernández-Escobar, Z. U. Rahman, H. Yilmazer, M. Kawasaki, C. J. Boehlert, *Philosophical Magazine* **2019**, 99, 557.

[26] J.-K. Han, T. Herndon, J.-i. Jang, T. G. Langdon, M. Kawasaki, *Advanced Engineering Materials* **2020**, 22, 1901289.

[27] K. Edalati, R. Uehiro, K. Fujiwara, Y. Ikeda, H.-W. Li, X. Sauvage, R. Z. Valiev, E. Akiba, I. Tanaka, Z. Horita, *Materials Science and Engineering: A* **2017**, 701, 158.

[28] D. Hernández-Escobar, R. R. Unocic, M. Kawasaki, C. J. Boehlert, *Journal of Alloys and Compounds* **2020**, 831, 154891.

[29] S. O. Rogachev, S. A. Nikulin, A. B. Rozhnov, V. M. Khatkevich, T. A. Nechaykina, M. V. Gorshenkov, R. V. Sundeev, *Metallurgical and Materials Transactions A* **2017**, 48, 6091.

[30] Y. Sun, M. Aindow, R. J. Hebert, T. G. Langdon, E. J. Lavernia, *Journal of Materials Science* **2017**, 52, 12170.

[31] B. Ahn, A. P. Zhilyaev, H.-J. Lee, M. Kawasaki, T. G. Langdon, *Materials Science and Engineering: A* **2015**, 635, 109.

[32] S. O. Rogachev, R. V. Sundeev, V. M. Khatkevich, *Materials Letters* **2016**, 173, 123.

[33] S. O. Rogachev, S. A. Nikulin, V. M. Khatkevich, R. V. Sundeev, A. Komissarov, *Metallurgical Materials Transactions A* **2020**, 51, 1781.

[34] B. L. Mordike, T. Ebert, *Materials Science and Engineering: A* **2001**, 302, 37.

[35] J. Hirsch, T. Al-Samman, *Acta Materialia* **2013**, 61, 818.

[36] X. Li, X. Liu, S. Wu, K. W. K. Yeung, Y. Zheng, P. K. Chu, *Acta Biomaterialia* **2016**, 45, 2.

[37] A. Atrens, S. Johnston, Z. Shi, M. S. Dargusch, *Scripta Materialia* **2018**, 154, 92.

[38] B. Elambharathi, S. D. Kumar, V. U. Dhanoop, S. Dinakar, S. Rajumar, S. Sharma, V. Kumar, C. Li, E. M. T. Eldin, S. Wojciechowski, *Heliyon* **2022**, 8, e11712.

[39] J. Song, J. Chen, X. Xiong, X. Peng, D. Chen, F. Pan, *Journal of Magnesium and Alloys* **2022**, 10, 863.

[40] A. Atrens, G.-L. Song, M. Liu, Z. Shi, F. Cao, M. S. Dargusch, *Adv. Eng. Mater.* **2015**, 17, 400.

[41] G. Wu, C. Wang, M. Sun, W. Ding, *Journal of Magnesium and Alloys* **2021**, 9, 1.

[42] L. L. Rokhlin, *Magnesium Alloys Containing Rare Earth Metals: Structure and Properties* CRC Press, London **2003**.

[43] A. Imandoust, C. D. Barrett, T. Al-Samman, K. A. Inal, H. El Kadiri, *Journal of Materials Science* **2017**, 52, 1.

[44] R. B. Figueiredo, P. R. Cetlin, T. G. Langdon, *Materials Science and Engineering: A* **2011**, 528, 8198.

[45] R. B. Figueiredo, P. H. R. Pereira, M. T. P. Aguilar, P. R. Cetlin, T. G. Langdon, *Acta Materialia* **2012**, 60, 3190.

[46] K. Edalati, Z. Horita, T. G. Langdon, *Scripta Materialia* **2009**, 60, 9.

[47] F. Wetscher, A. Vorhauer, R. Stock, R. Pippan, *Materials Science and Engineering: A* **2004**, 387-389, 809.

[48] Y. Mikami, K. Oda, M. Kamaya, M. Mochizuki, *Materials Science and Engineering: A* **2015**, 647, 256.

[49] J.-H. Cho, A. D. Rollett, K. H. Oh, *Metallurgical and Materials Transactions A* **2005**, 36, 3427.

[50] R. Hielscher, H. Schaeben, *J. Appl. Cryst.* **2008**, 41, 1024.

[51] N. Bayat Tork, S. H. Razavi, H. Saghafian, R. Mahmudi, *Adv. Eng. Mater.* **2016**, 18, 156.

[52] N. Azizi, R. Mahmudi, *Materials Science and Engineering: A* **2021**, 817, 141385.

[53] Y. Lu, Y. Huang, J. Bode, C. Vogt, R. Willumeit-Römer, K. U. Kainer, N. Hort, *Adv. Eng. Mater.* **2022**, 24, 2200966.

[54] O. Sitdikov, R. Kaibyshev, T. Sakai, *Materials Science Forum* **2003**, 419-422, 521.

[55] C. Xie, J. M. He, B. W. Zhu, X. Liu, J. Zhang, X. F. Wang, X. D. Shu, Q. H. Fang, *International Journal of Plasticity* **2018**, 111, 211.

[56] S. Tighiouaret, A. Hanna, H. Azzeddine, L. Rabahi, A. Dakhouche, F. Brisset, A.-L. Helbert, T. Baudin, D. Bradai, *Materials Chemistry and Physics* **2021**, 267, 124598.

[57] S. Sadi, A. Hanna, H. Azzeddine, C. Casas, T. Baudin, A.-L. Helbert, F. Brisset, J. M. Cabrera, *Materials Characterization* **2021**, 181, 111454.

[58] F. Guerza-Soualah, A. Hanna, H. Azzeddine, A.-L. Helbert, F. Brisset, T. Baudin, D. Bradai, *Materials Today Communications* **2020**, 24, 101239.

[59] S. Sandlöbes, I. Schestakow, S. B. Yi, S. Zaefferer, J. Q. Chen, M. Friák, J. Neugebauer, D. Raabe, *Materials Science Forum* **2011**, 690, 202.

[60] M. R. Barnett, M. D. Nave, C. J. Bettles, *Materials Science and Engineering: A* **2004**, 386, 205.

[61] M. M. Castro, S. Sabbaghianrad, P. H. R. Pereira, E. M. Mazzer, A. Isaac, T. G. Langdon, R. B. Figueiredo, *Journal of Alloys and Compounds* **2019**, 804, 421.

[62] Y. I. Bourezg, H. Azzeddine, T. Baudin, A.-L. Helbert, Y. Huang, D. Bradai, T. G. Langdon, *Materials Science and Engineering: A* **2018**, 724, 477.

[63] Y. Huang, R. Figueiredo, T. Baudin, A.-L. Helbert, F. Brisset, T. G. Langdon, *Materials Research* **2013**, 16, 577.

[64] R. Kocich, L. Kunčická, P. Král, T. C. Lowe, *Materials & Design* **2016**, 90, 1092.